

# Hall instability: origin, properties, and asymptotic theory for its tearing mode

Leonid Kitchatinov<sup>1,2†</sup>

<sup>1</sup>Institute of Solar-Terrestrial Physics SB RAS, Lermontov Str. 126A, 664033, Irkutsk, Russia

<sup>2</sup>Pulkovo Astronomical Observatory, St. Petersburg, 196140, Russia

(Received xx; revised xx; accepted xx)

Hall instability in electron magnetohydrodynamics is interpreted as the shear-Hall instability driven jointly by helicoidal oscillations and shear in the electron current velocity. This explanation suggests an antiparallel orientation of the background magnetic field and vorticity of the current velocity as the necessary condition for Hall instability. The condition is tested and generally confirmed by numerical computations in plane slab geometry. Unstable eigenmodes are localized in the spatial regions of the antiparallel field and vorticity. Computations of the tearing-type mode of the instability are complemented by (and generally agree with) asymptotic analytical estimations for large Hall numbers. The stabilizing effect of perfect conductor boundary conditions is found and explained. For large Hall numbers, the growth rates approach the power law dependence  $\sigma \propto B^\alpha \eta^{1-\alpha}$  on the magnetic field ( $B$ ) and diffusivity ( $\eta$ ). Almost all computations give the power index  $\alpha = 3/4$  with one exception of the tearing-type mode with vacuum boundary conditions for which case  $\alpha = 2/3$ .

## 1. Introduction

The Hall effect is studied mainly in relation to its ability to catalyze the dissipation of magnetic fields. This effect conserves magnetic energy and magnetic helicity but it can amplify resistive dissipation by decreasing the spatial scale of magnetic structures. Goldreich & Reisenegger (1992) noted that hypothetical Hall turbulence can accelerate the decay of magnetic fields in a neutron star crust towards their observationally detected rates; the Hall cascade has been studied numerically by Hollerbach & Rüdiger (2002) and Brandenburg (2020). Vainshtein *et al.* (2000) considered a similar effect for the solar corona.

Alternatively, dissipative magnetic structures can be produced by instabilities. Growth rates of hydromagnetic tearing instability are known to increase with allowance for the Hall effect (see Zhang *et al.* 2017; Shi *et al.* 2020; Bora *et al.* 2021, for recent publications). This is probably because the Hall effect can drive its own instability of the tearing type.

Hall instability was discovered by Rheinhardt & Geppert (2002). They found that the Hall effect can destabilize an equilibrium magnetic field if second-order spatial derivatives of the field do not vanish. The instability requires inhomogeneity in the background state for its development but can onset under diverse conditions. If the background state includes reversals of magnetic field, the instability can operate in the tearing mode (Gourgouliatos & Hollerbach 2016). Reversals are however not necessary and an inhomogeneous background field without reversals can be unstable as well (Rheinhardt & Geppert 2002; Pons & Geppert 2010). Inhomogeneity of density also can

† Email address for correspondence: kit@izf.irk.ru

facilitate the instability (Rheinhardt *et al.* 2004; Wood *et al.* 2014). It is not clear at the moment whether the instabilities driven by the Hall effect under these diverse conditions are of the same origin. There is no commonly accepted pictorial explanation of Hall instability/instabilities.

A possible explanation was proposed in the preceding paper (Kitchatinov 2017). The explanation relies on analogy with shear-Hall instability (cf. Sect. 8.4.3 in Rüdiger & Hollerbach 2004; Kunz 2008) and suggests that the Hall instability results from shear in the electron current velocity. This paper tests the explanation by computations of the Hall instability in the electron MHD approximation in plane pinch geometry.

The next Section 2 briefly reminds the essence of the Hall effect and the proposed explanation for Hall instability. Section 3 describes the design and equations of the model. Section 4 presents the results of numerical and analytical estimations for the Hall instability of the background field profiles with and without reversal of the field direction. The final Section 5 summarizes the results and concludes.

## 2. Hall effect and Hall instability

The Hall effect is related to the magnetically induced anisotropy of electric conductivity. If the gyrofrequency  $\omega_e$  of electrons - the main carriers of electric current - is not small compared to the frequency  $\nu_{ei}$  of electron collisions with particles of other species, the conductivity  $\sigma_{\parallel}$  along the magnetic field lines is larger than conductivities for other directions. The Ohm's law then reads (see, e.g., Somov 2013, Chapt.11)

$$\mathbf{j}' = \frac{\sigma_{\parallel}}{1 + R_{\text{H}}^2} \left[ \mathbf{E}' + R_{\text{H}} \hat{\mathbf{b}} \times \mathbf{E}' + R_{\text{H}}^2 \hat{\mathbf{b}} (\hat{\mathbf{b}} \cdot \mathbf{E}') \right], \quad (2.1)$$

where  $\hat{\mathbf{b}}$  is the unit vector along the magnetic field  $\mathbf{B}$ ,  $\mathbf{j} = c(\nabla \times \mathbf{B})/(4\pi)$  is the current density,  $\mathbf{E}$  is the electric field, the primed notations mean that the equation is formulated for the reference frame co-moving with the fluid mass velocity  $\mathbf{u}$ , and

$$R_{\text{H}} = \omega_e/\nu_{ei} \quad (2.2)$$

is the Hall number. Equation (2.1) can be reversed to express the electric field in terms of the current density:

$$\mathbf{E}' = \left( \mathbf{j}' - R_{\text{H}} \hat{\mathbf{b}} \times \mathbf{j}' \right) / \sigma_{\parallel}. \quad (2.3)$$

If equation (2.3) is used instead of its isotropic counterpart  $\mathbf{E}' = \mathbf{j}'/\sigma_{\parallel}$  in the standard derivation of the induction equation of MHD (see, e.g., Parker 1979, Chapter 4), the derivation yields

$$\frac{\partial \mathbf{B}}{\partial t} = \nabla \times [(\mathbf{u}_c + \mathbf{u}) \times \mathbf{B} - \eta \nabla \times \mathbf{B}], \quad (2.4)$$

where  $\eta = c^2/(4\pi\sigma_{\parallel})$  is the magnetic diffusivity,

$$\mathbf{u}_c = -\mathbf{j}'/(en_e) \quad (2.5)$$

is the current velocity, and the expressions for the gyrofrequency  $\omega_e = eB/(m_e c)$  and conductivity  $\sigma_{\parallel} = e^2 n_e / (m_e \nu_{ei})$  in terms of the microscopic plasma parameters are used. The Hall effect in MHD, therefore, means an additional current velocity (2.5) for the magnetic field advection.

This effect for a uniform background field together with a (prescribed) plane shear flow can drive an instability. The sufficient condition for the shear-Hall instability is a

counter-alignment of the magnetic field and shear-flow vorticity (Rüdiger & Hollerbach 2004; Rüdiger & Kitchatinov 2005). The shear-Hall instability allows a clear pictorial explanation in terms of the combined action of shear in the mass velocity and helicoidal oscillations induced by the Hall effect (see discussion of fig.8 in Kunz 2008).

As the current velocity  $\mathbf{u}_c$  enters equation (2.4) in the same way as the mass velocity  $\mathbf{u}$ , it should lead to the same consequences. Instability can be expected from shear in the current velocity if its vorticity is counter-aligned to the magnetic field. This is the interpretation of the Hall instability supposed in this paper. The interpretation can explain the diversity of conditions for which the Hall instability is met. It is clear why the magnetic field should depend at least quadratically on position for the instability (Rheinhardt & Geppert 2002): otherwise the current velocity has no shear. It is also clear why density inhomogeneity can be relevant. Inhomogeneous electron density in Eq. (2.5) can be the reason for a shear. The magnetic field and current vorticity are counter-aligned near the local maxima of the (unidirectional) magnetic field. This explains why reversals of the field direction are not necessary for the instability.

The difference with the shear-Hall instability however is that the unstable background field is necessarily inhomogeneous and the current shear does not change the magnetic energy. This results in the diffusive character of the Hall instability. Its growth rates scale as  $B^\alpha \eta^{1-\alpha}$  with  $0 < \alpha < 1$  for the large Hall number.

### 3. The model

We adopt the electron MHD approximation that omits the mass velocity  $\mathbf{u}$  in the induction equation (2.4). The approximation is justified for the solid crust of neutron stars and possibly for the case of large microscopic viscosity compared to the magnetic diffusivity. The case of large magnetic Prandtl number is characteristic of the hot plasmas of stellar coronae (Brandenburg & Subramanian 2005, Sect. 3). Normalized variables are used with distances normalized to the characteristic scale  $L$  of the background field, the field strength normalized with the amplitude  $B_0$  of this field, and time measured in diffusive units  $L^2/\eta$ . With this approximation and normalization, the induction equation retains only one governing parameter of the Hall number (2.2) that is now defined with (constant) amplitude  $B_0$  of the background field:

$$\frac{\partial \mathbf{B}}{\partial t} = \nabla \times [R_H \mathbf{B} \times (\nabla \times \mathbf{B}) - \nabla \times \mathbf{B}]. \quad (3.1)$$

We use a Cartesian coordinate system and consider the stability of the magnetic field that has only one non-zero  $z$  component and varies with coordinate  $x$  only,

$$\mathbf{B} = (0, 0, B(x)). \quad (3.2)$$

The linear stability of this background field to small disturbances  $\mathbf{B}'$  is considered. In all cases where instability is found, the most rapidly growing modes are uniform along the  $y$ -axis. The (toroidal)  $y$ -component  $b(x, z)$  and (poloidal) component  $\nabla \times (\hat{\mathbf{y}} a(x, z))$  normal to this axis are convenient to distinguish in such 2D disturbances to satisfy automatically the condition  $\nabla \cdot \mathbf{b} = 0$  ( $\hat{\mathbf{y}}$  is the unit vector along the  $y$ -axis)

$$\mathbf{B}'(x, z) = \hat{\mathbf{y}} b(x, z) + \nabla \times (\hat{\mathbf{y}} a(x, z)). \quad (3.3)$$

The equation system for the small disturbances can be obtained by linearization of Eq. (3.1). Coefficients of the resulting equations do not depend on time or  $z$ . An exponential dependence on these variables  $b, a \propto \exp(\sigma t + ikz)$  can therefore be assumed

that leads to the eigenvalue problem:

$$\begin{aligned}\sigma a &= -ikR_{\text{H}}B(x)b - k^2a + \frac{\partial^2 a}{\partial x^2}, \\ \sigma b &= ikR_{\text{H}}\left[B(x)\left(\frac{\partial^2 a}{\partial x^2} - k^2a\right) - \frac{\partial^2 B}{\partial x^2}a\right] - k^2b + \frac{\partial^2 b}{\partial x^2}.\end{aligned}\quad (3.4)$$

The second derivative of the background field accounts for the shear in the current velocity. The neglect of the diffusive decay of this field is justified if the growth rates of instability are large,  $\text{Re}(\sigma) \gg 1$ .

The equations (3.4) are solved in a plane slab with two boundaries imposed at  $x = \pm 1$ . Unless otherwise stated, the results to follow correspond to the vacuum conditions at the slab boundaries,

$$b = 0, \quad \frac{\partial a}{\partial x} = \mp ka \quad \text{for } x = \pm 1. \quad (3.5)$$

A finite background field at the boundaries for this case can be understood as imposed by external sources. The conditions for perfect conductor boundaries,

$$\frac{\partial b}{\partial x} = 0, \quad a = 0 \quad \text{for } x = \pm 1, \quad (3.6)$$

is an alternative possibility.

Numerical computations were performed with a uniform finite-difference grid of 750 grid-points. As the unstable eigenmodes can include a fine spatial structure, a fourth-order accurate finite difference scheme was used for spatial derivatives.

## 4. Results

The eigenmodes of Eq.(3.4) include the well-known helicoidal oscillations. No overstable solutions were found however. All the modes with positive growth rates have zero imaginary part of their eigenvalues.

According to the proposed explanation for the instability, it can be expected for the antiparallel orientation of the background magnetic field and vorticity of the current velocity (2.5). For the 1D profiles of Eq.(3.2) this means the inequality

$$B(x)\frac{\partial^2 B(x)}{\partial x^2} < 0. \quad (4.1)$$

We proceed by testing this condition with computations for different field profiles. The cases of symmetric and antisymmetric profiles about the slab midplane can be distinguished.

### 4.1. Antisymmetric field profiles

#### 4.1.1. Numerical computations

Antisymmetric profiles  $B(x) = -B(-x)$  can support unstable modes of the tearing-type. We first test the profile

$$B(x) = \sin(-\pi x/2), \quad (4.2)$$

which satisfies the condition (4.1).

Figure 1 shows the growth rates of the most unstable modes and the wave numbers for which these maximum growth rates are obtained. For a large Hall number, the growth rate approaches the power law  $\sigma \propto R_{\text{H}}^{2/3}$  in agreement with Gourgouliatos & Hollerbach (2016).

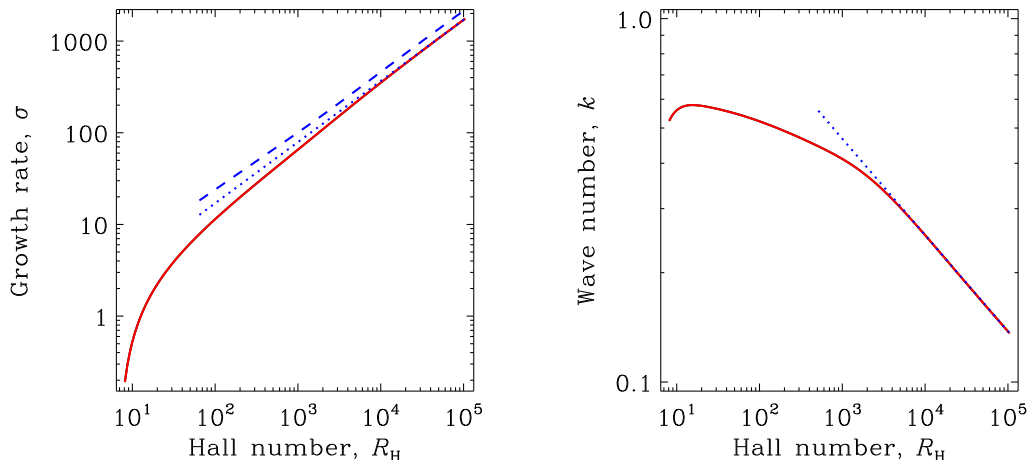


FIGURE 1. *Left panel*: Growth rate of the most rapidly growing mode for the field profile of Eq. (4.2). The dotted line indicates the power law dependence  $\sigma \propto R_H^{2/3}$  for large  $R_H$ . The dashed line shows the result of analytical asymptotic estimation of the next Section. *Right panel*: The wave number for which the maximum growth rate is attained. The power law approximation  $k \propto R_H^{-0.265}$  is shown by the dotted line. All for the vacuum boundary condition (3.5).

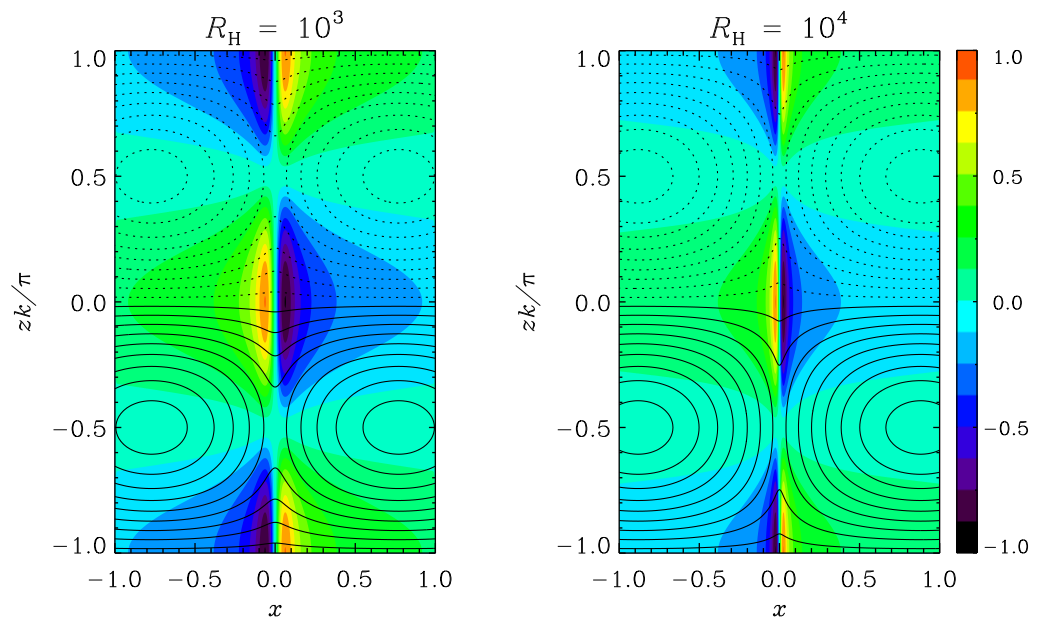


FIGURE 2. Poloidal field lines and isolines of the toroidal field of most rapidly growing modes for  $R_H = 10^3$  (*left panel*) and  $R_H = 10^4$  (*right panel*). Full and dashed lines correspond to the clockwise and anti-clockwise circulation of the poloidal field vector respectively. All for the field profile of Eq. (4.2).

Figure 2 shows the eigenmode structure for two large values of the Hall number. Reconnection of the field lines in a region near the  $x = 0$  position of the background field reversal is evident from this figure. The thickness of the reconnection layer decreases with the Hall number. The wave numbers of Fig. 1 are smaller than one. Antisym-

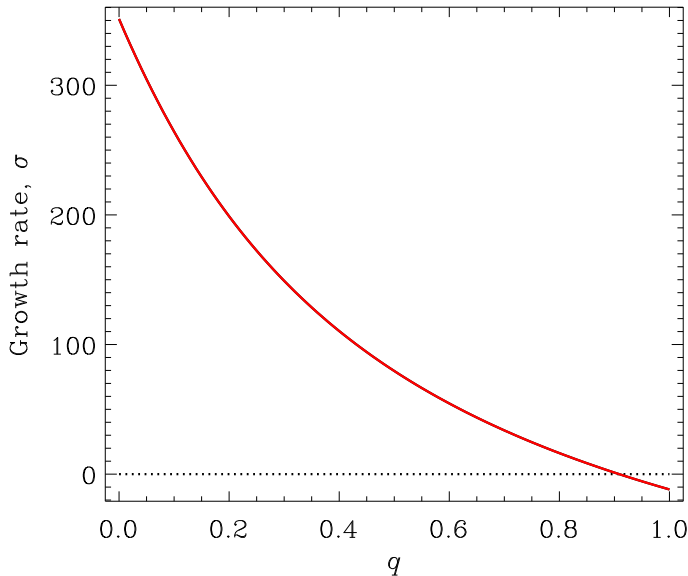


FIGURE 3. Dependence of the growth rate on the  $q$ -parameter of the profile  $B(x) = (1 - q) \sin(-\pi x/2) - qx$ .  $R_H = 10^4$ ,  $k = 0.25$ .

metric field profiles can be unstable to the long wavelength tearing-type disturbances (Gourgouliatos & Hollerbach 2016).

Not all antisymmetric profiles are unstable however. Figure 3 shows the growth rate as the function of the  $q$ -parameter of the profile  $B(x) = (1 - q) \sin(-\pi x/2) - qx$ . The growth rate reverses to negative values for  $q \rightarrow 1$ . The current velocity for the linear profile of  $q = 1$  is uniform and has no shear. The condition of Eq. (4.1) is then violated and the instability is switched off.

The local condition is also not sufficient for the global instability. The instability is switched off with a change to the perfect conductor boundary conditions (3.5). This is probably because the helicoidal oscillation takes part in the instability (Kitchatinov 2017). The helicoidal rotation is blocked by superconducting boundaries.

The growth rate scaling with the Hall number depends on the model design also. Kitchatinov (2017) considered a periodic background field in unbounded space. The profile of Eq. (4.2) is mirror-symmetric about the planes of  $x = \pm 1$  when considered in unbounded space. The eigenmodes for this periodic profile have to possess the same symmetry. This means that  $x$ -derivatives of the eigenfunctions should be zero at  $x = \pm 1$ . The case of the periodic profile (4.2) in unbounded space can therefore be reproduced in the slab model of this paper with the ‘periodic’ boundary conditions

$$\frac{\partial a}{\partial x} = \frac{\partial b}{\partial x} = 0 \text{ for } x = \pm 1. \quad (4.3)$$

The results for these conditions are shown in Fig. 4. They are similar to the case of the vacuum conditions but with different slopes in power law dependencies on the (large) Hall number. The power index in the dependence of the growth rate changes to  $3/4$  and the absolute value of the index for the wave number reduces about two times.

We proceed to analytical estimations of the instability to justify and partly explain the numerical results.

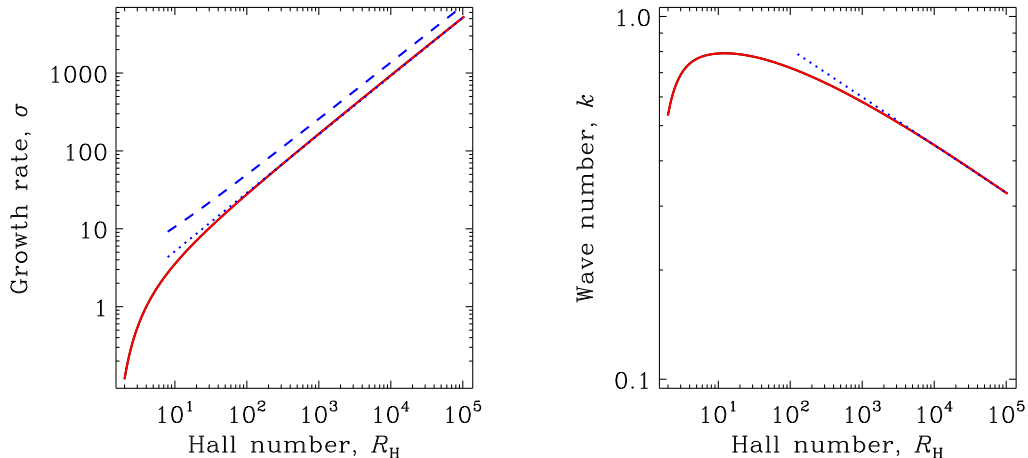


FIGURE 4. The same as in Fig. 1 but for periodic boundary conditions of Eq. (4.3). In this case, the asymptotic dependence of the growth rate on the Hall number changes to  $\sigma \propto R_H^{3/4}$ . The dashed line shows the result of analytical asymptotic estimation. Scaling for the wave number also changes to  $k \propto R_H^{-0.132}$ .

#### 4.1.2. Asymptotic estimation

The method of asymptotic analysis of resistive hydromagnetic instabilities was developed in the seminal paper by Furth *et al.* (1963). We apply this method to the tearing mode of the Hall instability at large  $R_H$ .

It is convenient to reformulate Eq. (3.4) in terms of new variables  $\gamma = \sigma/R_H$  and  $v = ikb/\gamma$ :

$$\begin{aligned} \gamma(a + Bv) &= \frac{1}{R_H} \left( \frac{\partial^2 a}{\partial x^2} - k^2 a \right), \\ \gamma^2 v &= -k^2 \left[ B \left( \frac{\partial^2 a}{\partial x^2} - k^2 a \right) - \frac{\partial^2 B}{\partial x^2} a \right] + \frac{\gamma}{R_H} \left( \frac{\partial^2 v}{\partial x^2} - k^2 v \right). \end{aligned} \quad (4.4)$$

The case of the large Hall number  $R_H \gg 1$  is considered.

The eigenmodes of Fig. 2 show a thin reconnection layer in the central part of the slab and smooth variations outside this layer. These two distinct regions are visualized more clearly by the eigenfunction profiles of Fig. 5. The recipe by Furth *et al.* (1963) is to solve for the (central) diffusive and (outer) non-diffusive regions separately. Dispersion relation for the growth rates then results from a link of these solutions.

The unstable eigenmodes grow with ‘hybrid’ rates that are large compared with the rate of diffusion but small compared to the helicoidal oscillation frequency,

$$R_H^{-1} \ll \gamma \ll 1. \quad (4.5)$$

With these inequalities, Eqs. (4.4) for the non-diffusive regions reduce to

$$\begin{aligned} v &= -a/B \\ \frac{\partial^2 a}{\partial x^2} - \left( \frac{1}{B} \frac{\partial^2 B}{\partial x^2} + k^2 \right) a &= 0. \end{aligned} \quad (4.6)$$

The solution of this linear equation for the profile (4.2) and  $k \leq \pi/2$  includes two arbitrary constants,

$$a(x) = C (\sin(px) + C_1 \cos(px)), \quad (4.7)$$

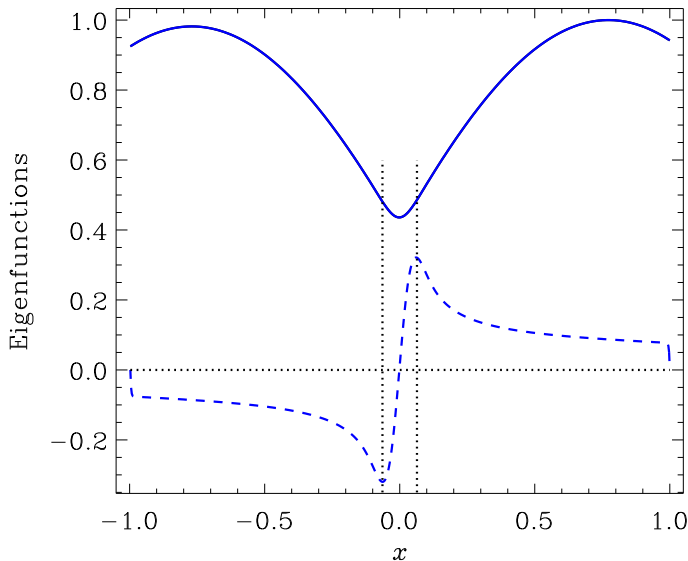


FIGURE 5. Profiles of the  $x$ -component of the current velocity  $\gamma v(x)$  (dashed) and  $a(x)$  (full line) of the tearing-type eigenmode for  $R_H = 10^3$ . The vertical dotted lines show the central diffusive layer.

where  $p = \sqrt{|\pi^2/4 - k^2|}$ . The constant  $C_1$  can be defined with boundary conditions that have to be applied separately for positive and negative  $x$ . The vacuum boundary condition (3.5) for positive  $x$  gives

$$C_1 = C_+ = \frac{k \sin(p) + p \cos(p)}{p \sin(p) - k \cos(p)}, \quad (4.8)$$

while for negative  $x$  it is  $C_1 = C_- = -C_+$ . The constant  $C$  in the ‘external’ solution (4.7) remains indefinite in the linear stability problem. However, the constant does not contribute the stability index

$$\Delta' = \frac{1}{a} \frac{\partial a}{\partial x} \Big|_{x=+0} - \frac{1}{a} \frac{\partial a}{\partial x} \Big|_{x=-0} \quad (4.9)$$

of Furth *et al.* (1963). It is accounted for in Eq. (4.9) that the logarithmic derivatives of the external solution vary little with  $|x| \ll 1$  on either side of the origin and their values at the borders of the diffusive layer can be replaced by the values at the origin.

With the Eq. (4.8) for the vacuum boundary conditions we get

$$\Delta' = 2p \frac{p \sin(p) - k \cos(p)}{k \sin(p) + p \cos(p)}. \quad (4.10)$$

This expression changes from positive to negative values with  $k$  increasing beyond the value of about  $k = 1.263$ . We shall see that the negative values mean stability (note that the wave numbers of Fig.1 correspond to positive  $\Delta'$ ). Repeating the derivations for  $k > \pi/2$  gives the (negative) quantity

$$\Delta' = -2p \frac{(k+p) \exp(2p) + k - p}{(k+p) \exp(2p) - k + p}, \quad (4.11)$$

to which the  $\Delta'$  of Eq. (4.10) transforms continuously when  $k$  exceeds  $\pi/2$ .



Repeating the derivations for periodic conditions of Eq. (4.3) we find positive

$$\Delta' = 2p \tan(p) \quad (4.12)$$

for  $k \leq \pi/2$  and negative  $\Delta' = -2p[\exp(2p) - 1]/[\exp(2p) + 1]$  for  $k > \pi/2$ .

It can be shown that  $\Delta'$  for perfect conductor boundary conditions or the linear profile of  $B$  is negative for any  $k$  thus confirming numerically found stability for these cases.

Inside the ‘inner’ diffusive region, spatial derivatives are not small  $\partial/\partial x \gg 1$ . The region is also thin so that the the background field can be approximated by the linear profile  $B(x) = xB'$ , where the prime means the derivative at  $x = 0$ . Eqs. (4.4) then reduce to

$$\begin{aligned} \gamma \left( a - \frac{\pi}{2} xv \right) &= \frac{1}{R_H} \frac{\partial^2 a}{\partial x^2} \\ \gamma^2 v &= k^2 x \frac{\pi}{2} \frac{\partial^2 a}{\partial x^2} + \frac{\gamma}{R_H} \frac{\partial^2 v}{\partial x^2}, \end{aligned} \quad (4.13)$$

where  $B' = -\pi/2$  for the profile (4.2) was used; a generalization to any other antisymmetric profile is easy.

An expression for the jump in the logarithmic derivative across the diffusion layer

$$\Delta(\gamma) = \frac{1}{a} \frac{\partial a}{\partial x} \Big|_{x=\delta} - \frac{1}{a} \frac{\partial a}{\partial x} \Big|_{x=-\delta} \quad (4.14)$$

should be derived from Eqs. (4.13) to get the dispersion relation  $\Delta(\gamma) = \Delta'$ .

The  $\Delta(\gamma)$  is derived in the so-called ‘constant  $\psi$  approximation’ (Furth *et al.* 1963; Priest 2014, Sect. 6.8.1) in Appendix A. Eq. (A 17) leads to the following estimation for the growth rate

$$\sigma = R_H \left( -k + \sqrt{k^2 + 1.18 \Delta'(k) k^{3/2} R_H^{-1/2}} \right), \quad (4.15)$$

where positive  $\Delta'$  only result in positive growth rates. The growth rates estimated with this equation are shown by the dashed lines in Figs. 1 and 4 for the vacuum and periodic boundary conditions respectively. The  $\Delta'$  of the corresponding equations (4.10) and (4.12) were used in the estimations with the wave numbers taken from the corresponding figures. In contrast with the numerical computations, the asymptotic estimations apply to large Hall numbers only but are not restricted to the moderately large  $R_H$ .

The analytic and numerical trends are similar and they approach each other with increasing Hall number. The asymptotic theory overestimates the numerical growth rates by about 20% for the largest Hall numbers in Fig. 1 and by almost 30% in Fig. 4. The difference can be related to the approximate nature of the asymptotic theory. The clear similarity of the analytic and numerical results nevertheless confirms the numerically detected dependence of the Hall instability scaling on boundary conditions. The asymptotic estimations also confirm the stability of the linear profile of the background field and the stability for perfect conductor boundary conditions in our model.

#### 4.2. Symmetric field profiles

According to the proposed interpretation of the Hall instability, it can be expected if the condition of Eq. (4.1) is satisfied. The expectation is generally confirmed by computations for the parabolic profile

$$B(x) = \beta - x^2. \quad (4.16)$$

In agreement with the condition (4.1), instability was found for positive  $\beta$  only. It can be expected that the local condition should be satisfied in a sufficiently broad region and the

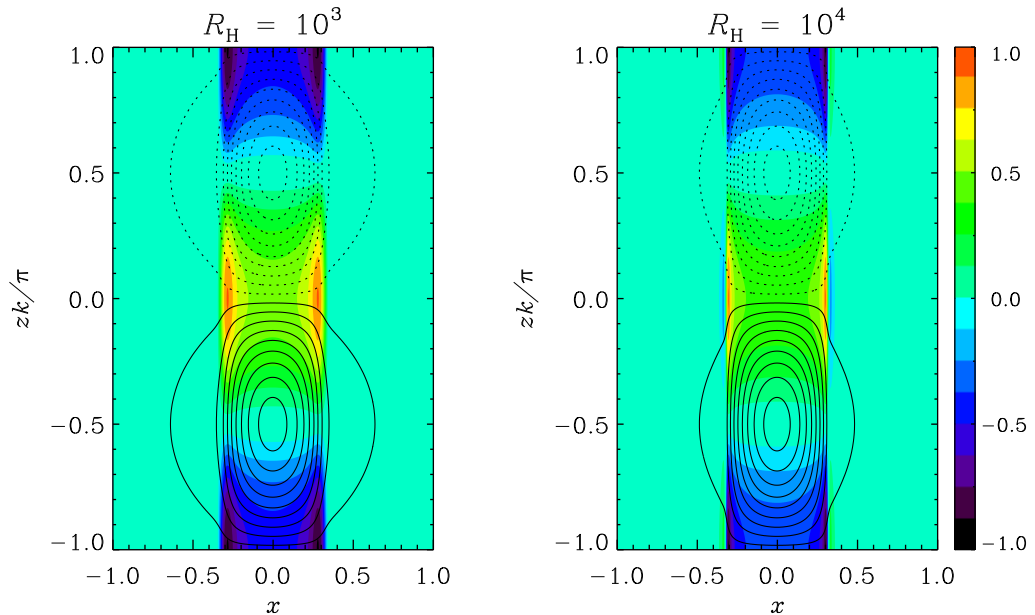


FIGURE 6. Poloidal field lines and isolines of the toroidal field of most rapidly growing instability modes for  $R_H = 10^3$  (left panel) and  $R_H = 10^4$  (right panel). Full and dashed lines correspond to the clockwise and anti-clockwise circulation of the poloidal field vector respectively. All for the symmetric field profile of Eq. (4.16) with  $\beta = 0.1$ .

parameter  $\beta$  should be sufficiently large for the onset of the instability. The expectation is generally confirmed by computations, but the critical value  $\beta_c$  for the instability is rather small and decreases with the Hall number:  $\beta_c \approx 5 \times 10^{-3}$  for  $R_H = 10^3$  and  $\beta_c \approx 3 \times 10^{-4}$  for  $R_H = 10^5$ . The condition (4.1) is fulfilled in the region of  $-\beta^{1/2} < x < \beta^{1/2}$ .

Figure 6 shows that unstable eigenmodes are confined to this region.

The modes of this Figure do not belong to the tearing type but possess a fine structure near the border of the instability region. The region broadens with increasing  $\beta$  and occupies the entire slab for  $\beta = 1$  (Fig. 7). Another difference from the antisymmetric field profile, for which only one unstable mode was found for a given  $k$ , is that two unstable modes symmetric and antisymmetric about the slab midplane can exist for the symmetric profile of Eq. (4.16). These two types of symmetry are illustrated by Fig. 7. The antisymmetric mode always had a smaller growth rate compared to the symmetric mode.

The maximum growth rates for  $\beta = 0.1$  and  $\beta = 1$  are shown in Fig. 8 as functions of the Hall number. The growth rates approach the power law of  $\sigma \propto R_H^{3/4}$  for large Hall number. The asymptotic growth rates depend weakly on  $\beta$  but the asymptotic trend is approached at larger  $R_H$  for smaller  $\beta$ .

The perfect conductor boundary conditions (3.6) switch the instability off for  $\beta = 1$  similar to the case of the antisymmetric field profile. For small  $\beta$  however, the instability is weakly sensitive to the boundary conditions, though the growth rates for perfect conductor boundaries are somewhat smaller compared to the vacuum conditions. This is probably because the unstable modes for small  $\beta$  occupy the central part of the slab only (Fig. 6) and do not feel the boundaries.

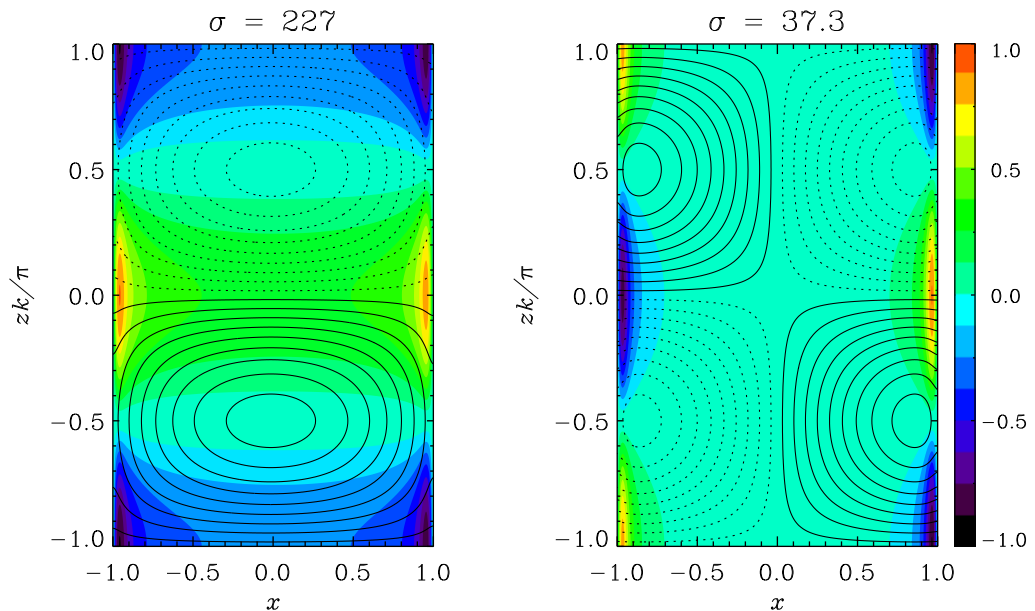


FIGURE 7. Poloidal field lines and isolines of the toroidal field for the symmetric (*left panel*) and antisymmetric (*right panel*) instability modes. The corresponding normalized growth rates are given at the top. All for the symmetric profile of Eq. (4.16) with  $\beta = 1$  and  $R_H = 10^3$ .

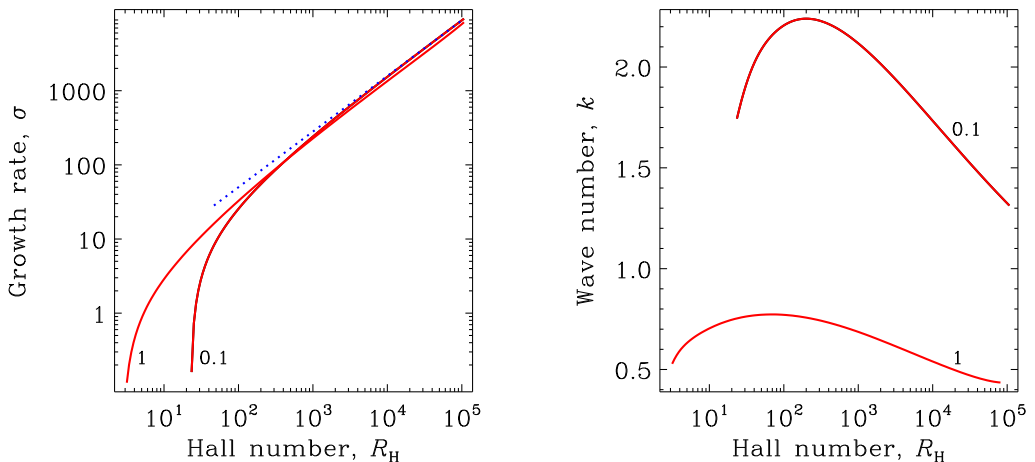


FIGURE 8. *Left panel*: Growth rates for the symmetric field profile of Eq. (4.16) with  $\beta = 0.1$  and  $\beta = 1$ . The dotted line shows the asymptotic power-law dependence  $\sigma \propto R_H^{3/4}$ . *Right panel*: Wave numbers for which the maximum growth rates of the left panel were obtained. The lines are marked by the corresponding values of  $\beta$ .

## 5. Discussion

The formerly proposed interpretation of the Hall instability as driven jointly by the helicoidal rotation and shear in the current velocity (Kitchatinov 2017) is generally confirmed by the computations of this paper. According to this interpretation, instability is expected for the background field profiles having a region of counter-aligned magnetic field and vorticity of the current velocity. For 1D profiles of this paper, this means that inequality (4.1) should be satisfied for instability. The inequality is satisfied by the

antisymmetric profile (4.2) supporting the tearing-type mode of the instability. However, the instability is switched off when the antisymmetric linear profile with uniform current velocity is approached (Fig. 3). Figure 6 shows that unstable modes for the symmetric field are restricted to the region where the inequality (4.1) is satisfied.

The proposed interpretation also explains the diffusive character of the instability. The helicoidal rotation pushes the magnetic field lines in the direction of decreasing field strength and therefore decreasing rate of this rotation. The instability in the region of the relatively strong field is blocked by the less unstable regions of the weaker field. This ‘displacements jam’ is resolved by diffusion. This picture can also explain the instability switch off by the perfect conductor boundary conditions: the superconducting walls block helicoidal rotation. The numerical results for the tearing mode are confirmed by independent asymptotic estimations. The analytical estimations confirm in particular the stabilizing effect of superconducting boundaries.

This stabilizing effect is probably not of a general nature. It can be expected to weaken for ‘sufficiently broad’ profiles of the background field tending to constant far away from the location of the field reversal. Are the broad profiles realistic however? The Hall instability can be relevant to the release of magnetic energy from small-scale magnetic structures. The structures have neither vacuum no superconducting boundaries but are surrounded by other similar structures. The periodic conditions of Eq. (4.3) seem to be more adequate for this case.

The growth rates approach asymptotically the power law dependence  $\sigma \propto R_H^\alpha$  on the Hall number with  $\alpha = 3/4$ ;  $\alpha = 2/3$  for the case of the tearing mode with vacuum boundary conditions. This means that the growth rate in physical units scales as  $\sigma \propto B^\alpha \eta^{1-\alpha}$ . The growth rate of the Hall instability increases more steeply with the magnetic field compared to the hydromagnetic tearing instability with  $\alpha = 1/2$ . The Hall instability can produce current sheets without magnetic reconnection (Fig. 6). The instability gives an additional channel for the release of magnetic energy complementary to the canonical tearing mode. Hall instability catalyzes resistive dissipation by decreasing spatial scale of magnetic field. It may be pertinent to note that the Hall number (2.2) does not include any spatial scale. A decrease of the field scale cannot therefore be balanced by diffusion. Release of magnetic energy on nonlinear stage of the instability proceeds in a sequence of spikes or bursts, each spike releases several percent of magnetic energy (Kitchatinov 2017, 2019).

The condition of the counter-aligned magnetic field and vorticity of the current velocity can be written as

$$\mathbf{B} \cdot (\nabla \times (\nabla \times \mathbf{B})) > 0 \quad (5.1)$$

for 3D fields. This heuristic condition for the instability is satisfied by any force-free field of  $\nabla \times \mathbf{B} = \alpha(\mathbf{r})\mathbf{B}$ . Instability of a 1D force-free field with maximum helicity was confirmed in Kitchatinov (2019). The instability can be active with the force-free fields of the solar corona where the Hall number  $R_H \sim 10^7$  is large.

This work was financially supported by the Ministry of Science and High Education of the Russian Federation and by the Russian Foundations for Basic Research (Project 19-02-00088). The author is thankful to Ms Jennifer Sutton for language editing.

Declaration of Interests. The author reports no conflict of interest.

## Appendix A. Derivation of $\Delta(\gamma)$

Equations (4.13) for the diffusive layer can be simplified with the redefined variables  $\tilde{v} = \pi v/2$ ,  $\tilde{\gamma} = 2\gamma/(\pi k)$ , and  $\tilde{R} = k\pi R_H/2$ :

$$\frac{\partial^2 a}{\partial x^2} = \tilde{R}\tilde{\gamma}(a - x\tilde{v}), \quad (\text{A } 1)$$

$$\tilde{\gamma}^2\tilde{v} = x\frac{\partial^2 a}{\partial x^2} + \frac{\tilde{\gamma}}{\tilde{R}}\frac{\partial^2 \tilde{v}}{\partial x^2}. \quad (\text{A } 2)$$

Integration of Eq. (A 1) across the diffusive layer yields the  $\Delta$ -parameter of Eq. (4.14),

$$\Delta = \frac{\tilde{\gamma}\tilde{R}}{a(\delta)} \int_{-\delta}^{\delta} (a(x) - x\tilde{v}(x)) dx, \quad (\text{A } 3)$$

where  $\delta \ll 1$  is a small distance outside of the diffusive layer and it is taken into account that  $a(x)$  profile is symmetric with  $a(\delta) = a(-\delta)$  (Fig. 5).

Substitution of  $\partial^2 a/\partial x^2$  from Eq. (A 1) into Eq. (A 2) gives the differential equation

$$\frac{\partial^2 \tilde{v}}{\partial s^2} - s^2\tilde{v} - \tilde{\gamma}\tilde{v} = -\tilde{R}^{1/2}sa, \quad (\text{A } 4)$$

in terms of a new variable  $s = \tilde{R}^{1/2}x$

The idea with the constant  $\psi$  approximation - constant  $a$  in the present case - is to express  $\tilde{v}$  in terms of  $a$  using the Eq. (A 4) and then put  $a$  outside the integral of Eq. (A 3) based on the fact that it varies little inside the diffusive layer (Fig. 5). This excludes the (still unknown) constant  $a$  from the expression for  $\Delta$  and gives the expression in terms of the parameters  $\gamma$ ,  $R_H$  and  $k$ , as desired.

Applying this approximation to Eq. (A 3) and using the new variable  $s$  gives

$$\Delta = \tilde{R}^{1/2}\tilde{\gamma} \int_{-\tilde{R}^{1/2}\delta}^{\tilde{R}^{1/2}\delta} \left(1 - \frac{s}{a\tilde{R}^{1/2}}\tilde{v}(s)\right) ds. \quad (\text{A } 5)$$

It may be noted that each of the two terms of the integral in this expression diverge with increasing Hall number but the two diverging terms almost balance each other to combine into a finite quantity.

The operator on the left-hand side of Eq. (A 4) has the Hermite functions,

$$\varphi_n(s) = \frac{(-1)^n}{\pi^{1/4}\sqrt{2^n n!}} e^{s^2/2} \frac{d^n}{ds^n} e^{-s^2}, \quad (\text{A } 6)$$

as its eigenfunctions:

$$\frac{d^2\varphi_n}{ds^2} - s^2\varphi_n = -(2n+1)\varphi_n. \quad (\text{A } 7)$$

The functions make up a complete (orthogonal and normalized) basis that can be used for solving the equation (A 4) in terms of the series expansion

$$\tilde{v}(s) = a\tilde{R}^{1/2} \sum_{n=0}^{\infty} \frac{\varphi_n(s)}{2n+1+\tilde{\gamma}} \int_{-\infty}^{\infty} \varphi_n(s')s'ds'. \quad (\text{A } 8)$$

Note that the solution for not constant  $a$  can be obtained by placing  $a$  under the integral sign on the right-hand side of Eq. (A 8).

Expansion of the entire integrand in Eq. (A 5) in terms of the Hermite functions and

using Eq. (A 8) give

$$\Delta = \tilde{R}^{1/2}\tilde{\gamma} \sum_{n=0}^{\infty} \left[ \left( \int_{-\infty}^{\infty} \varphi_n(s) ds \right)^2 - \frac{1}{2n+1+\tilde{\gamma}} \left( \int_{-\infty}^{\infty} s\varphi_n(s) ds \right)^2 \right], \quad (\text{A } 9)$$

where the integration limits are changed to infinity for the asymptotic case of  $\tilde{R} \gg \delta^{-2}$ .

The symmetry relation  $\varphi_n(s) = (-1)^n \varphi_n(-s)$  shows that the first term under the summation sign in Eq. (A 9) is zero for odd  $n$  and the second term is zero for even  $n$ . The equation can then be written as

$$\Delta = \tilde{R}^{1/2}\tilde{\gamma} \sum_{m=0}^{\infty} \left[ \left( \int_{-\infty}^{\infty} \varphi_{2m}(s) ds \right)^2 - \frac{1}{4m+3+\tilde{\gamma}} \left( \int_{-\infty}^{\infty} s\varphi_{2m+1}(s) ds \right)^2 \right], \quad (\text{A } 10)$$

and the relations

$$\int_{-\infty}^{\infty} s \varphi_{2m+1}(s) ds = \sqrt{4m+2} \int_{-\infty}^{\infty} \varphi_{2m}(s) ds \quad (\text{A } 11)$$

and

$$\left( \int_{-\infty}^{\infty} \varphi_{2m}(s) ds \right)^2 = 2 \frac{\Gamma(m+1/2)}{\Gamma(m+1)} \quad (\text{A } 12)$$

can be used to simplify it further:

$$\Delta = 2\tilde{R}^{1/2}\tilde{\gamma} \sum_{m=0}^{\infty} \frac{1+\tilde{\gamma}}{4m+3+\tilde{\gamma}} \frac{\Gamma(m+1/2)}{\Gamma(m+1)}, \quad (\text{A } 13)$$

where  $\Gamma$  is the Gamma function.

As has been noted, each of the two series on the right-hand side of Eq. (A 10) diverges when summed-up separately, but their combination of Eq. (A 13) converges ( $\Gamma(m+1/2)/\Gamma(m+1) \propto m^{-1/2}$  for large  $m$ ). The convergence is however slow and Eq. (A 13) is difficult to handle. The series in this equation can be rearranged in order to extract its slowly converging part that can be summed-up analytically and the remaining rapidly converging part is easy for numerical estimation:

$$\Delta = 2\sqrt{\pi\tilde{R}}\tilde{\gamma}(1+\tilde{\gamma}) \sum_{n=0}^{\infty} (-1)^n \tilde{\gamma}^n A_n, \quad (\text{A } 14)$$

where

$$A_n = \sum_{m=0}^{\infty} \frac{C_m}{(4m+3)^{(n+1)}}, \quad C_0 = 1, \quad \text{and} \quad C_m = \frac{2m-1}{2m} C_{m-1} \quad \text{for } m > 0. \quad (\text{A } 15)$$

The geometric series expansion of the term  $1/(4m+3+\tilde{\gamma})$  in Eq. (A 13) in powers of  $\tilde{\gamma}/(4m+3)$  served to derive the Eqs (A 14) and (A 15). The first four coefficients in the series of Eq. (A 14) read

$$A_0 = \sqrt{\pi} \frac{\Gamma(3/4)}{\Gamma(1/4)} = 0.59907, \quad A_1 = 0.12856, \quad A_2 = 0.03897, \quad A_3 = 0.01259, \quad (\text{A } 16)$$

where the last three coefficients were evaluated numerically from their rapidly converging series of Eq. (A 15).

Equation (A 14) gives the expansion for  $\Delta$  in powers of the asymptotically small parameter  $\tilde{\gamma}$ . Cutting the expansion after the second-order terms gives

$$\Delta = 0.847 \sqrt{\frac{R_H}{k^3}} (\gamma^2 + 2k\gamma), \quad (\text{A } 17)$$

where we returned to the ‘unwaved’ parameters of Sect. 4.1.2.

## REFERENCES

- BORA, K., BHATTACHARYYA, R. & SMOLARKIEWICZ, P. K. 2021 Evolution of Three-dimensional Coherent Structures in Hall Magnetohydrodynamics. *ApJ* **906** (2), 102.
- BRANDENBURG, A. 2020 Hall Cascade with Fractional Magnetic Helicity in Neutron Star Crusts. *ApJ* **901** (1), 18.
- BRANDENBURG, A. & SUBRAMANIAN, K. 2005 Astrophysical magnetic fields and nonlinear dynamo theory. *Physics Reports* **417** (1-4), 1–209.
- FURTH, H. P., KILLEEN, J. & ROSENBLUTH, M. N. 1963 Finite-Resistivity Instabilities of a Sheet Pinch. *Physics of Fluids* **6** (4), 459–484.
- GOLDREICH, P. & REISENEGGER, A. 1992 Magnetic Field Decay in Isolated Neutron Stars. *ApJ* **395**, 250–258.
- GOURGOULIATOS, K. N. & HOLLERBACH, R. 2016 Resistive tearing instability in electron MHD: application to neutron star crusts. *MNRAS* **463** (3), 3381–3389.
- HOLLERBACH, R. & RÜDIGER, G. 2002 The influence of Hall drift on the magnetic fields of neutron stars. *MNRAS* **337** (1), 216–224.
- KITCHATINOV, L. 2019 Stability of a force-free Hall equilibrium and release of magnetic energy. *Astronomische Nachrichten* **340** (6), 475–482.
- KITCHATINOV, L. L. 2017 Double Hall instability: A catalyzer of magnetic energy release. *Astronomy Letters* **43** (9), 624–633.
- KUNZ, M. W. 2008 On the linear stability of weakly ionized, magnetized planar shear flows. *MNRAS* **385** (3), 1494–1510.
- PARKER, E. N. 1979 *Cosmical magnetic fields: Their origin and their activity*. Clarendon Press, Oxford.
- PONS, J. A. & GEPPERT, U. 2010 Confirmation of the occurrence of the Hall instability in the non-linear regime. *A&A* **513**, L12.
- PRIEST, E. 2014 *Magnetohydrodynamics of the Sun*. Cambridge University Press.
- RHEINHARDT, M. & GEPPERT, U. 2002 Hall-Drift Induced Magnetic Field Instability in Neutron Stars. *Phys. Rev. Lett.* **88** (10), 101103.
- RHEINHARDT, M., KONENKOV, D. & GEPPERT, U. 2004 The occurrence of the Hall instability in crusts of isolated neutron stars. *A&A* **420**, 631–645.
- RÜDIGER, G. & HOLLERBACH, R. 2004 *The magnetic universe: geophysical and astrophysical dynamo theory*. WILEY-VCH, Weinheim.
- RÜDIGER, G. & KITCHATINOV, L. L. 2005 The influence of the Hall effect on the global stability of cool protostellar disks. *A&A* **434** (2), 629–635.
- SHI, C., VELLI, M., PUCCI, F., TENERANI, A. & INNOCENTI, M. E. 2020 Oblique Tearing Mode Instability: Guide Field and Hall Effect. *ApJ* **902** (2), 142.
- SOMOV, B. V. 2013 *Plasma Astrophysics, Part I*. Springer Science+Business Media, New York.
- VAINSHTAIN, S. I., CHITRE, S. M. & OLINTO, A. V. 2000 Rapid dissipation of magnetic fields due to the Hall current. *Phys. Rev. E* **61** (4), 4422–4430.
- WOOD, T. S., HOLLERBACH, R. & LYUTIKOV, M. 2014 Density-shear instability in electron magneto-hydrodynamics. *Physics of Plasmas* **21** (5), 052110.
- ZHANG, W., MA, Z. W. & WANG, S. 2017 Hall effect on tearing mode instabilities in tokamak. *Physics of Plasmas* **24** (10), 102510.